

## RESEARCH ARTICLE

10.1002/2015JA021697

## Key Points:

- Westward traveling surge (WTS) is reproduced by global magnetohydrodynamic (MHD) simulation
- WTS is embedded in upward field-aligned current generated by vorticities in the near-Earth region
- WTS is structured by space charge deposited by divergence of Hall current in the ionosphere

## Correspondence to:

Y. Ebihara,  
ebihara@rsh.kyoto-u.ac.jp

## Citation:

Ebihara, Y., and T. Tanaka (2015), Substorm simulation: Formation of westward traveling surge, *J. Geophys. Res. Space Physics*, 120, 10,466–10,484, doi:10.1002/2015JA021697.

Received 17 JUL 2015

Accepted 12 NOV 2015

Accepted article online 14 NOV 2015

Published online 21 DEC 2015

## Substorm simulation: Formation of westward traveling surge

Y. Ebihara<sup>1</sup> and T. Tanaka<sup>2</sup>

<sup>1</sup>Research Institute for Sustainable Humanosphere, Kyoto University, Kyoto, Japan, <sup>2</sup>International Center for Space Weather Science and Education, Kyushu University, Fukuoka, Japan

**Abstract** Auroral substorm expansion is characterized by initial brightening of aurora, followed by a bulge expanding in all directions, and a westward traveling surge (WTS). On the basis of the result obtained by a global magnetohydrodynamic simulation, we propose a scenario for the onset and the subsequent formation of WTS. (1) Near-Earth neutral line releases magnetic tension in the near-Earth plasma sheet to compress plasma and accelerate it earthward. (2) Earthward, perpendicular flow is converted to parallel flow in the near-Earth tail region. (3) Plasma moves earthward parallel to a field line. The plasma pressure is additionally enhanced at off-equator with an expanding slow-mode variation. (4) Flow vorticities coexist near the off-equatorial high-pressure region. Resultant field-aligned current (FAC) is connected to the ionosphere, which may manifest initial brightening. (5) Due to continued earthward flow, the high-plasma pressure region continues to expand to the east and west. (6) The ionospheric conductivity continues to increase in the upward FAC region, and the conductivity gradient becomes steeper. (7) The convergence of the Hall current gives rise to divergent electric field near the steep gradient of the conductivity. (8) Due to the divergent electric field, magnetospheric plasma moves counterclockwise at low altitude (in the Northern Hemisphere). (9) The additional flow vorticity generates a localized upward FAC at low altitudes, which may manifest WTS, and redistributes the ionospheric current and conductivity. Thus, WTS may be maintained in a self-consistent manner, and be a natural consequence of the overflow of the Hall current.

### 1. Introduction

A sudden brightening of aurora around midnight is a noticeable feature at the beginning of substorm expansion phase. The aurora increases its intensity and expands in all directions [Akasofu, 1964; Akasofu *et al.*, 1965]. A spectacular structure that expands toward the evening is referred to as a westward traveling surge (WTS) [Akasofu, 1963, 1964; Akasofu *et al.*, 1965; Anger *et al.*, 1973; Craven *et al.*, 1989; Elphinstone *et al.*, 1995]. It traverses along the preexisting arc forming a poleward expanding bulge [Akasofu *et al.*, 1965]. According to observations, the WTS has the following characteristics: (1) intense inverted-V precipitation of electrons with energies of nearly  $\geq 10$  keV [Réme and Bosqued, 1973; Meng *et al.*, 1978; Shiokawa and Fukunishi, 1991; Fujii *et al.*, 1994; Olsson *et al.*, 1996; Cummer *et al.*, 2000], (2) intense upward field-aligned currents (FACs) on the poleward edge and inside the WTS [Kamide and Akasofu, 1975; Opgenoorth *et al.*, 1983; Shiokawa and Fukunishi, 1991; Fujii *et al.*, 1994; Marklund *et al.*, 1998; Cummer *et al.*, 2000], (3) a large southward electric field [Baumjohann and Opgenoorth, 1984; Fujii *et al.*, 1994; Marklund *et al.*, 1998], (4) a large westward electric field [Robinson and Vondrak, 1990], (5) counterclockwise plasma flow at the surge head [Weimer *et al.*, 1994], (6) a downward FAC poleward of the WTS [Fujii *et al.*, 1994; Marklund *et al.*, 1998; Cummer *et al.*, 2000], (7) the surge moves westward after the first contact of the poleward expanding bulge with a poleward boundary arc [Lyons *et al.*, 2013], (8) a presence of proton precipitation in a bulge while an absence of proton precipitation inside the WTS [Akasofu *et al.*, 1969; Fukunishi, 1975; Kadokura *et al.*, 2002], and irregular poleward motion [Rostoker *et al.*, 1987].

The generation of the localized upward FAC is the key to understanding the WTS. Several mechanisms have been proposed for the generation of the upward FAC that manifests the WTS. The Cowling channel model [Boström, 1975] suggests that very localized, intense upward FAC is formed on the western edge of the high-conductance region to satisfy the current continuity in the ionosphere [Baumjohann *et al.*, 1981; Inhester *et al.*, 1981; Baumjohann, 1983]. Kan *et al.* [1984] suggested the importance of blockages of the Hall current. A partial blockage results in the divergent electric field in the ionosphere. The convection pattern is redistributed in the ionosphere, and electrons are accelerated earthward to carry the intense upward FAC. On the basis of the Cowling channel model [Baumjohann *et al.*, 1981; Inhester *et al.*, 1981; Baumjohann, 1983], a feedback instability model is proposed [Rothwell *et al.*, 1984, 1988].

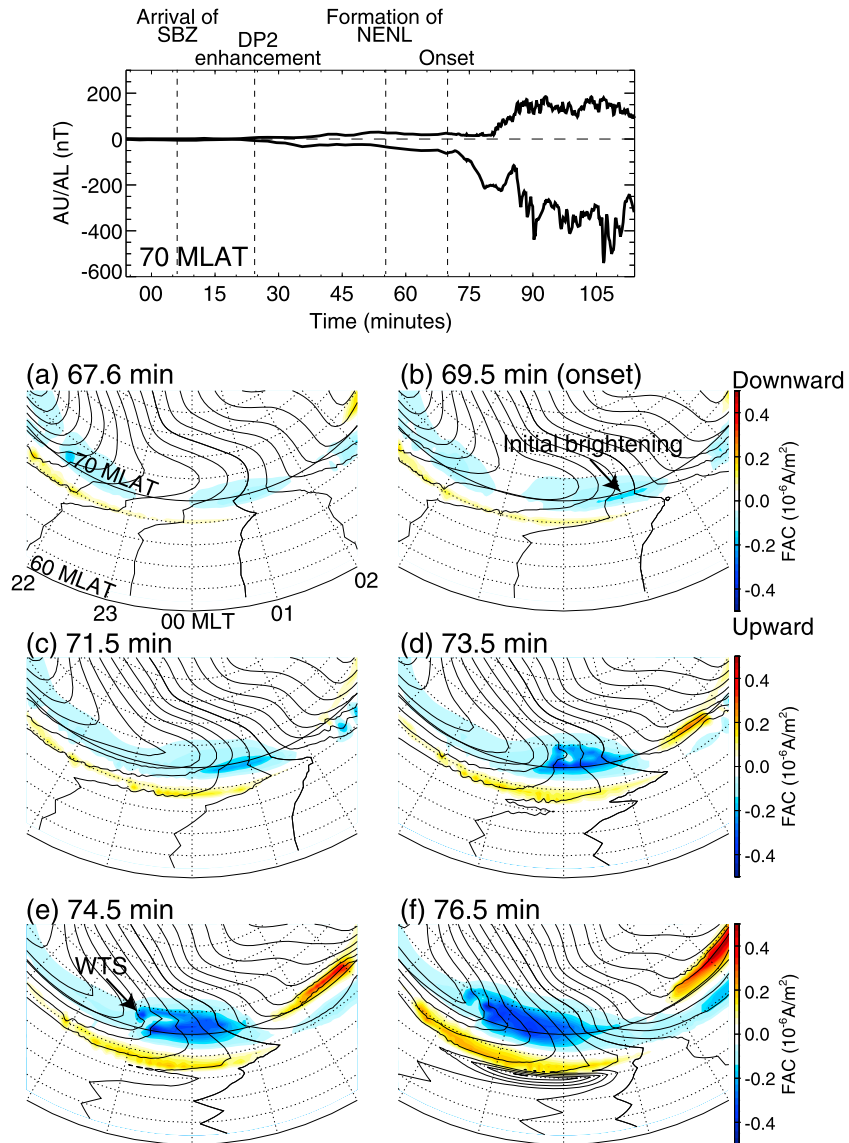


**Figure 1.** Field-aligned current at the ionosphere (positive downward). The contour indicates the ionospheric electric potential with an interval of 2 kV. Sun is to the top. The calculated AU and AL indices are shown in the top.

In the magnetospheric counterpart, the upward FAC associated with the WTS is thought to belong to the current wedge as a diversion of the westward cross-tail current in the near-Earth plasma sheet [e.g., *McPherron et al.*, 1973; *Fujii et al.*, 1994; *Birn and Hesse*, 1996, 2013; *Birn et al.*, 1999, 2004; *Keiling et al.*, 2009; *Yao et al.*, 2012; *Lyons et al.*, 2013; *Kepko et al.*, 2014, and references therein]. The development of the surge is thought to be a projection of an expansion of the plasma sheet and an intrusion of the plasma sheet boundary layer (PSBL) into the tail lobe [*Akasofu et al.*, 1971; *Bythrow and Potemra*, 1987]. In this model, shear instability is expected to grow in the PSBL, resulting in the intrusion [*Bythrow and Potemra*, 1987].

Many previous discussions on the formation of WTS have been based on current continuity in the ionosphere and the ionospheric projection of the FAC from the magnetosphere along a magnetic field line. However, to understand the WTS, we first have to know the generation mechanisms of the FAC in the magnetosphere-ionosphere coupling system. The FAC is attached to the ionosphere by the vorticity or shear motion of plasma, so we have to know the motion of magnetospheric plasma. Second, we have to know the current closure between the ionosphere and the magnetosphere. It is not guaranteed that the current line is always aligned with the magnetic field line. Usually, a current line is diverted from

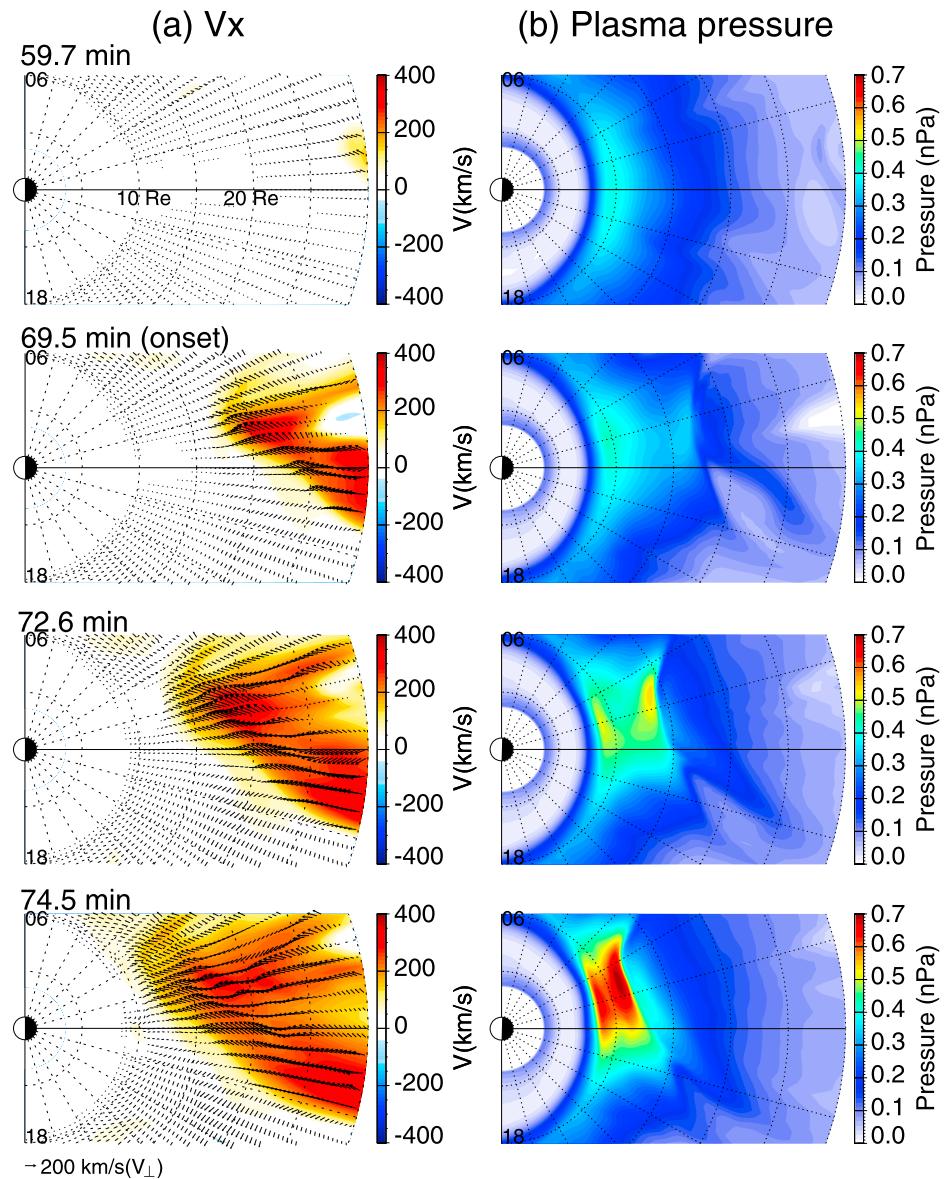


**Figure 2.** (a) X component of the plasma bulk flow and (b) plasma pressure in the equatorial plane. Initial brightening takes place at  $t = 69.5$  min. Sun is to the left. The arrow indicates the perpendicular plasma flow velocity.

the magnetic field line due to the perpendicular current as pointed out by *Tanaka et al.* [2010]. Thus, it is too straightforward to connect the WTS and the westward cross-tail current by a magnetic field line directly. The purpose of this study is an attempt to understand the mechanisms of the WTS in terms of the generation of FAC and current closure by using the global magnetohydrodynamics (MHD) simulation that incorporates magnetosphere-ionosphere coupling.

*Ebihara and Tanaka* [2015], hereinafter referred to as Paper 1, dealt with rapid intensification of upward FAC at the beginning of the substorm expansion phase (hereinafter, simply referred to as an initial brightening). Based on the global MHD simulation, they explained the initial brightening as follows: (1) Associated with the development of the convection, a near-Earth neutral line (NENL) [*Nishida and Nagayama*, 1973; *Russell and McPherron*, 1973] releases magnetic tension to compress and accelerate plasma earthward. (2) Magnetic tension causes squeezing of plasma toward the inner magnetosphere along a field line [*Haerendel*, 2010; *Tanaka et al.*, 2010]. (3) The squeezing causes plasma pressure increase and generates slow-mode expansion. (4) The perpendicular bulk flow is converted to the parallel flow in the near-Earth tail region [*Birn et al.*, 2004;

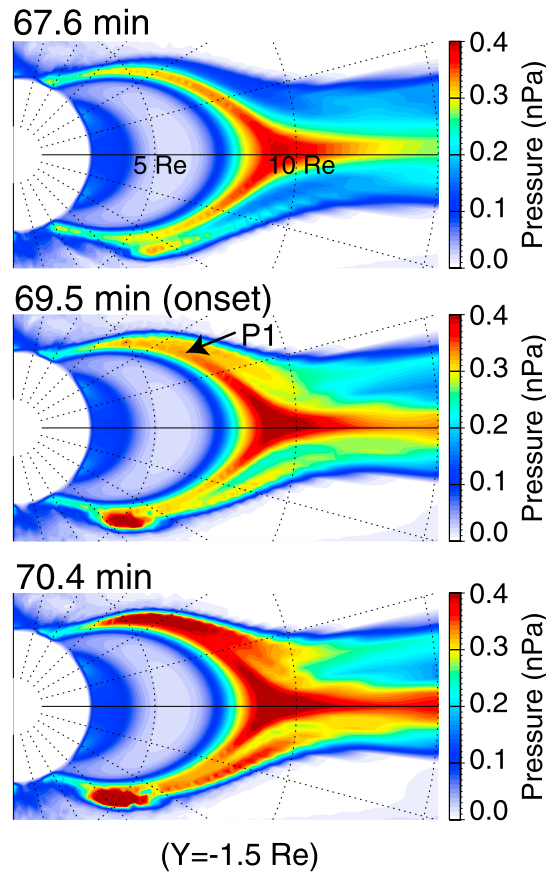


Figure 3. Plasma pressure in the X-Z plane at  $Y = -1.5 \text{ Re}$ . Sun is to the left.

on a spherical surface. The inner boundary of the magnetospheric domain was located at radial distance of 3 Re. We stacked 380 triangular prisms outward from the inner boundary so that the number of grid points was 46,572,278. The grid spacing in the X direction is 0.011, 0.13, and 0.32 Re at 3.0, 7.0, and 20 Re, respectively, at midnight in the equatorial plane. The grid spacing in the Z direction is 0.023, 0.072, and 0.20 Re, respectively. The number of grids was increased to improve the spatial resolution in comparison with that used in Paper 1. In Paper 1, Level 6 gridding was used.

The magnetosphere is coupled with the ionosphere by the following means. We calculated the parallel component of the current density at the inner boundary of the magnetosphere domain (at 3 Re). We mapped the parallel current, the plasma pressure, and temperature from the inner boundary of the magnetosphere domain to the ionosphere (at 1 Re) along the dipole magnetic field. We assumed that the height-integrated ionospheric conductivity is increased by the following three sources. The first source is associated with the ionization due to the solar extreme ultraviolet radiation. We used a functional form that depends on the solar zenith angle. The second source is associated with precipitation of accelerated particles (likely discrete auroras), which is a function of FAC. The contribution from the downward FAC is assumed to be 10 times lower than that from the upward FAC. The third source is associated with precipitation of scattered particles (likely diffuse auroras), which is assumed to be proportional to the square root of plasma pressure and to the temperature of magnetospheric plasma to the power of 1/4. The ionospheric current was calculated as

$$\mathbf{J}_i = \Sigma \mathbf{E}_i = - \begin{pmatrix} \Sigma_{\theta\theta} & \Sigma_{\theta\phi} \\ -\Sigma_{\theta\phi} & \Sigma_{\phi\phi} \end{pmatrix} \nabla \Phi_i, \quad (1)$$

where  $\mathbf{J}_i$  is the ionospheric current density,  $\Sigma$  is the height-integrated conductivity tensor,  $\mathbf{E}_i$  is the ionospheric electric field, and  $\Phi_i$  is the ionospheric electric potential.  $\theta$  and  $\phi$  represent colatitude and longitude

Tanaka et al., 2010]. (5) The plasma pressure further increases at off-equator. (6) Flow vortices are generated around the off-equatorial high-pressure region as a part of transition in the global convection. (7) A positive flow vortex generates the upward FAC that is directly connected to the ionosphere in the center of the Harang discontinuity. This paper focuses on the subsequent process until the formation of WTS.

## 2. Simulation Setup

In this study, we used the global MHD simulation developed by Tanaka [2015]. This simulation utilizes the grid system based on triangular prisms. First, we divided a spherical surface into 12 pentagons and then each pentagon was divided into 5 triangles, yielding a total of 60 triangles and 32 grid points. This is called Level 1 gridding. We further divided each triangle into 4 triangles to yield a total of 240 triangles and 122 grid points. This is called Level 2 gridding. Level 6 gridding was used in Paper 1, whereas Level 7 gridding was used in this simulation. In Level 7 gridding, the number of triangles was 245,760 and the number of grid points was 122,882

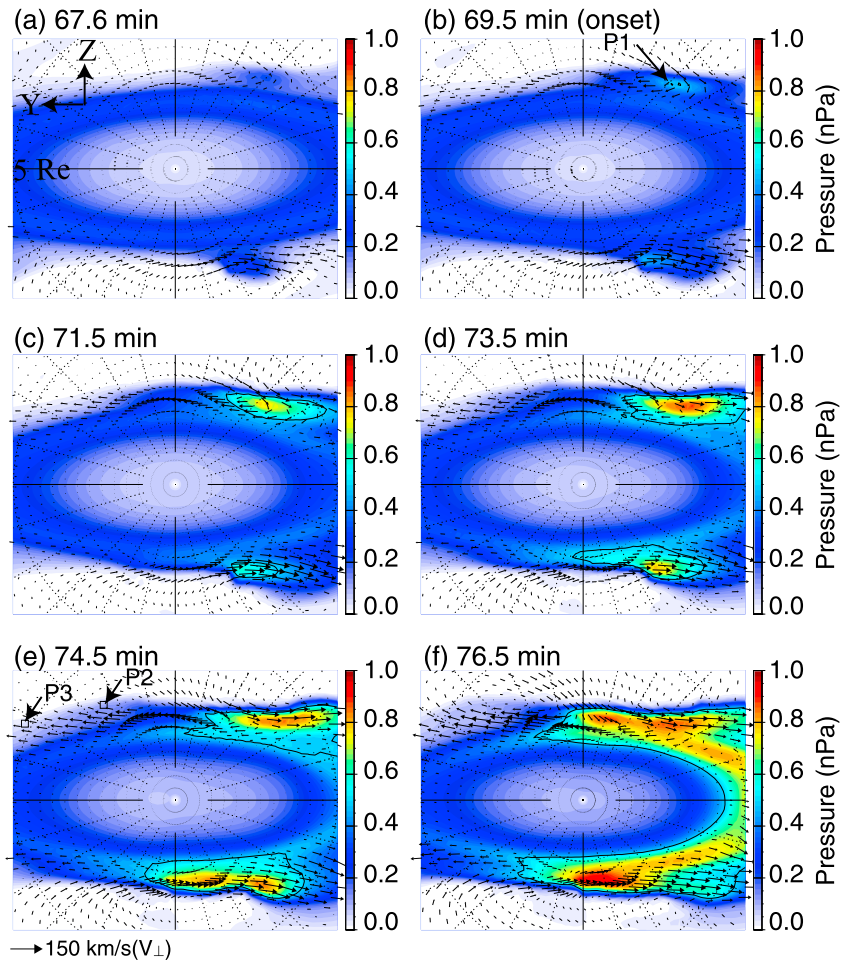


**Figure 4.** Plasma pressure in the Y-Z plane at  $X = -7 \text{ Re}$  (a) 67.6, (b) 69.5, (c) 71.5, (d) 73.5, (e) 74.5, (f) 76.5 min. The arrow indicates the perpendicular plasma flow in the Y-Z plane. The points labeled by M2 and M3 are connected to the wake of WTS and the leading edge of the WTS by a current line, respectively. The outer, dotted circle indicates 5 Re. Dusk is to the left.

in the spherical coordinates, respectively. The height-integrated conductivity tensor  $\Sigma$  is described by *Ebihara et al.* [2014] in detail. After calculating  $\Sigma$ , we solved an elliptic partial differential equation to obtain the ionospheric electric potential  $\Phi_i$  [e.g., *Tanaka*, 1994]. The ionospheric electric field was mapped to the inner boundary of the magnetosphere domain along the dipole magnetic field. The flow velocity corresponding to the mapped electric field was imposed to the magnetospheric plasma as a boundary condition of the magnetospheric domain of the simulation. Processes taking place in the gap between 1 Re and 3 Re, including Alfvén wave coupling between the ionosphere and the magnetosphere [e.g., *Vogt*, 2002; *Yoshikawa et al.*, 2011], were not taken into account. However, we believe that, by iterating the above loop many times, the force balance and current continuity condition are fully satisfied in the magnetosphere, and that the inconsistency could be resolved for a timescale being longer than a time step and Alfvén transit time between 1 Re and 3 Re. We focus on phenomena evolving on a timescale of a minute, whereas the time step of the computation is about 0.02 s.

We gave a simple boundary condition to the upstream of the solar wind. First, in order to obtain an almost steady state magnetosphere, we gave the solar wind a density of  $5.0 \text{ cm}^{-3}$ , a solar wind speed of 372 km/s, the Y component of the interplanetary magnetic field (IMF  $B_y$ ) of  $-2.5 \text{ nT}$ , and IMF  $B_z$  of 4.3 nT. Then we changed IMF  $B_z$  to  $-3.0 \text{ nT}$ . We defined  $t = 0$  to the moment at which the southward IMF reached  $X = 40 \text{ Re}$ . The southward IMF reached the bow shock at the subsolar point at  $t \approx 6 \text{ min}$ . The solar wind parameters used in Paper 1 were different from those used in this study, so that the locations of the NENL and the initial brightening are different. However, the underlying mechanism is essentially the same.

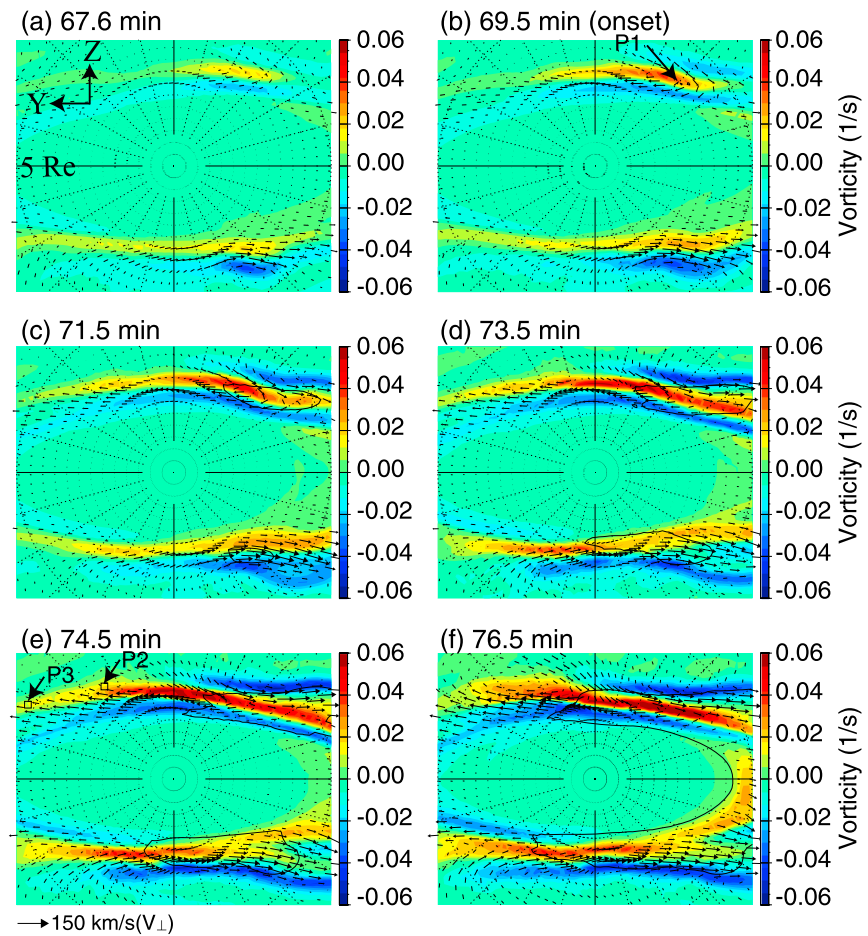


**Figure 5.** Same as Figure 4 except for parallel vorticity  $\Omega_{\parallel}$ . The black contour indicates the plasma pressure of 0.5 nPa.

### 3. Results

#### 3.1. Ionospheric Signatures of WTS

Figure 1 shows the time sequence of the calculated FAC distribution in the ionosphere together with the calculated  $AU/AL$  indices. The results show that the upward FAC (indicated by blue color) started to increase at a geomagnetic latitude of  $\approx 70^\circ$  and a geomagnetic longitude (MLT) of  $\approx 01$  h at  $t = 69.5$  min. This initial intensification of the upward FAC is elongated longitudinally and is quite similar to observations [e.g., Akasofu, 1964]. We call this variation initial brightening, and we call this moment onset of the auroral expansion. At  $t = 73.5$  min, the upward FAC region expands poleward and westward and exhibits fine structures. This feature may be referred to as the bulge [Akasofu, 1964]. At  $t = 74.5$  min, an elongated (arc-like) upward FAC continues to move westward. The upward FAC is intensified at the front of the bulge. The structure of the upward FAC may resemble the surge [Akasofu, 1964] or the WTS [Akasofu et al., 1965; Anger et al., 1973; Craven et al., 1989; Elphinstone et al., 1995]. Following Fujii et al. [1994], we calculated the net current ( $I_N$ ) and net Region 1-sense FAC ( $I_{R1}$ ) along a meridional line at 23 MLT (the leading edge of the WTS) at 74.5 min. The ratio  $I_N/I_{R1}$  is  $\sim 0.21$ , which may be consistent with the observation [Fujii et al., 1994], and may imply that the Region 1-sense FAC is not closed in the meridional plane on the leading edge of the WTS. WTS was not clearly identified in Paper 1 probably due to insufficient resolution of the simulation grid. The calculated  $AU$  and  $AL$  indices are shown in the top part of Figure 1. The sequence of magnetospheric and ionospheric processes is summarized as follows. The southward IMF arrived at the dayside magnetosheath at  $t \approx 6$  min. The DP2 ionospheric convection [Nishida, 1968] started to increase, and the  $AL$  index starts to decrease slightly at  $t \approx 24$  min. The near-Earth neutral line (NENL) forms at  $t \approx 56$  min. The initial brightening (sudden increase in the upward FAC near midnight) takes place at  $t = 69.5$  min, followed by a rapid decrease in the  $AL$  index. The sequence of the aurora taking place

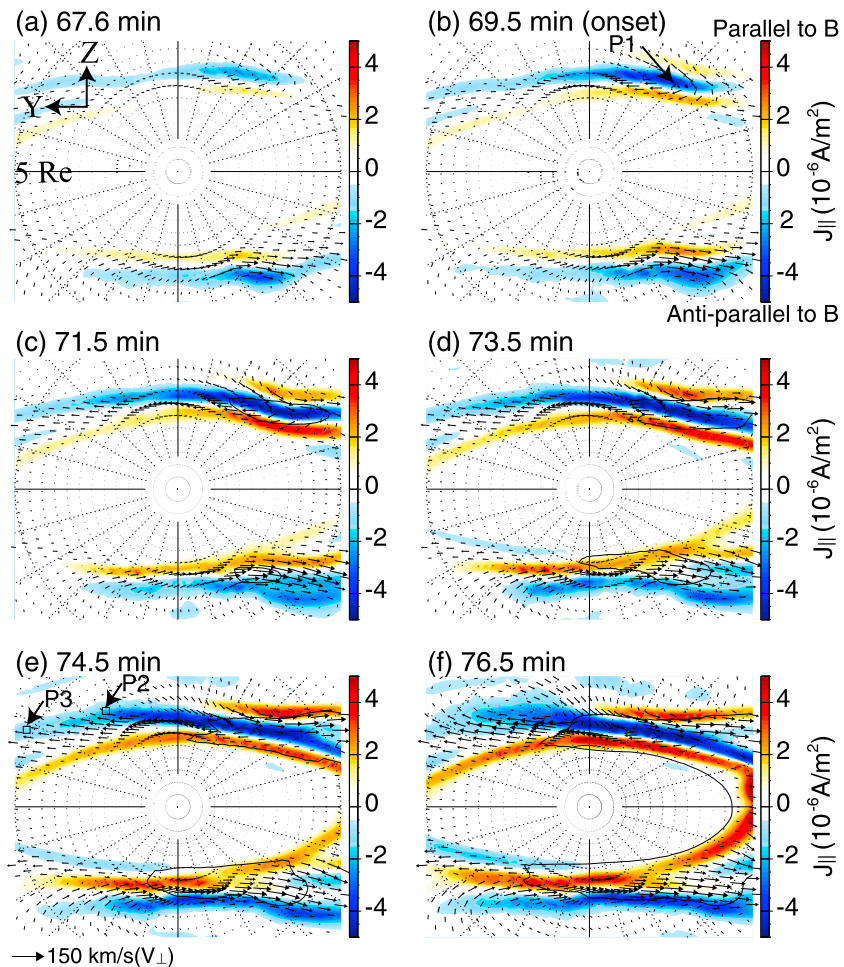


**Figure 6.** Same as Figure 4 except for the parallel component of the current density (field-aligned current)  $J_{\parallel}$ . The black contour indicates the plasma pressure of 0.5 nPa.

before the onset is described by Y. Ebihara and T. Tanaka (Substorm simulation: Quiet and N-S arcs preceding auroral breakup, submitted to *Journal of Geophysical Research*, 2015, referred to as Paper 2).

### 3.2. Magnetospheric Disturbances

Figure 2 is a summary of the  $X$  component of the plasma bulk flow ( $V_x$ ) and the plasma pressure ( $P$ ) in the equatorial plane. The results show that an NENL started to form at  $X \approx -42$  Re and  $t \approx 55$  min (Paper 2). The location of the NENL may be a bit far from that typically observed [e.g., *Nishida and Nagayama, 1973; Baker et al., 1996; Nagai et al., 1998; Ieda et al., 1998; Machida et al., 1999; Angelopoulos et al., 1994*]. After performing simulations with different solar wind conditions, we found that the location of the NENL depends on the solar wind conditions and their history, but that the location of the NENL does not essentially affect the result presented in this paper. The dependence of the location of the NENL on the solar wind conditions will be described in a separated paper. The formation of the NENL releases magnetic tension that accelerates plasma earthward in the near-Earth plasma sheet. The plasma pressure is enhanced by the squeezing [*Haerendel, 2010; Tanaka et al., 2010*]. The earthward flow appears to be braked at  $X \approx -17$  Re at  $t \approx 69.5$  min, which is referred to as flow braking. The flow braking results in the compression of the plasma and a further enhancement of the plasma pressure. Consequently, there are two pressure peaks. We call them the inner high-pressure region and the outer high-pressure region. After the onset, the high-speed earthward flow continues, and the region of the high-speed flow expands. This tendency is consistent with the statistical study of *Juusola et al. [2011]*. The plasma pressure also continues to increase in both the outer and inner high-pressure regions at  $t \approx 74.5$  min. The evolution of the plasma pressure is described by *Tanaka et al. [2010]*, and the mechanism of the initial brightening is explained by Paper 1 in more detail.

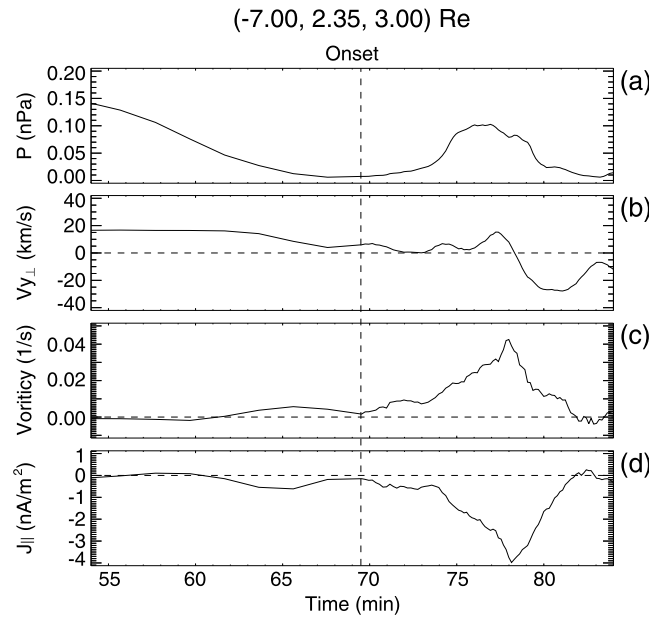


**Figure 7.** (a) Plasma pressure, (b) the Y component of the perpendicular flow, (c) the parallel vorticity, and (d) the field-aligned current (negative upward) at P2 (−7.00, 2.35, 3.00) Re. The vertical line indicates the onset.

Figure 3 shows the plasma pressure in the X-Z plane at  $Y = -1.5$  Re. The results show that the inner high-pressure region is concentrated near the equatorial plane at  $X \approx -9$  Re, which probably results from squeezing of the plasma due to tension force. In addition, a high-pressure region is also found at off-equator at  $|Z| \approx 3-4$  Re (Figure 3 P1). As described in Paper 1, the off-equatorial high-pressure region probably results from the conversion of the earthward perpendicular flow to parallel flow. The off-equatorial high-pressure region coexists with developing convection flow as if it pulls in and discharges ambient plasma, generating flow vorticities. In addition to the flow vorticities associated with global changes in the magnetospheric convection, the flow vorticities generate a pair of Region 1-sense FAC, causing the initial brightening (Paper 1). Due

to the continued earthward flow, the plasma pressure continues to increase at off-equator after the initial brightening.

Figure 4 is a time sequence of the plasma pressure in the Y-Z plane at  $X = -7$  Re. At  $t = 69.5$  min (onset), the plasma pressure appears to be enhanced at off-equator (Figure 4 P1). The pressure peak (Figure 4 P1) approximately corresponds to the off-equatorial high-pressure region (Figure 3 P1), which is responsible for generating the upward FAC that manifests the initial brightening (Paper 1). After the onset, the high-pressure region expanded westward and eastward. Westward flow is found in the westward portion of the off-equatorial high-pressure region. In Figure 4e (at 74.5 min), two points, labeled by P2 and P3, are marked by squares. These points are connected to the wake of the WTS and the leading edge of the WTS, respectively, by a current line. The region of the westward flow is shown to propagate westward, together with the expansion of the off-equatorial high-pressure region. The pressure distribution is not symmetric about the equatorial plane. The north-south asymmetry probably comes from a magnetic twist under the presence of the Y component of IMF [e.g., Cowley, 1981; Saita *et al.*, 2011]. The north-south asymmetry disappears when IMF  $B_y = 0$  (data not shown).

From the Ampère and Faraday laws, the generation of FAC is given by

$$\frac{\partial J_{\parallel}}{\partial t} = -\frac{1}{\mu_0} (\nabla \times \nabla \times \mathbf{E})_{\parallel}, \quad (2)$$

where  $\mathbf{E}$  is the electric field. When perturbations start with an initially uniform magnetic field, the following approximation can also be used [Paschmann *et al.*, 2002]:

$$\frac{\partial J_{\parallel}}{\partial t} = \frac{1}{\mu_0} \mathbf{B} \cdot \nabla \Omega_{\parallel}. \quad (3)$$

The parallel vorticity is given by  $\Omega_{\parallel} = \mathbf{B} \cdot (\nabla \times \mathbf{V})/B$ , where  $\mathbf{B}$  is the magnetic field, and  $\mathbf{V}$  is the velocity. This equation implies that the upward FAC ( $J_{\parallel} < 0$ ) is generated when the magnetospheric plasma is forced to rotate clockwise ( $\Omega_{\parallel} > 0$ ) at high altitude or counterclockwise ( $\Omega_{\parallel} < 0$ ) at low altitude (when viewed along a field line). Figure 5 is the same as Figure 4 except for the vorticity parallel to the magnetic field. At  $t = 69.5$  min (onset), the off-equatorial high-pressure region (Figure 4 P1) coexists with flow as if it pulls in ambient plasma from high latitude to the off-equatorial high-pressure region and discharges it westward

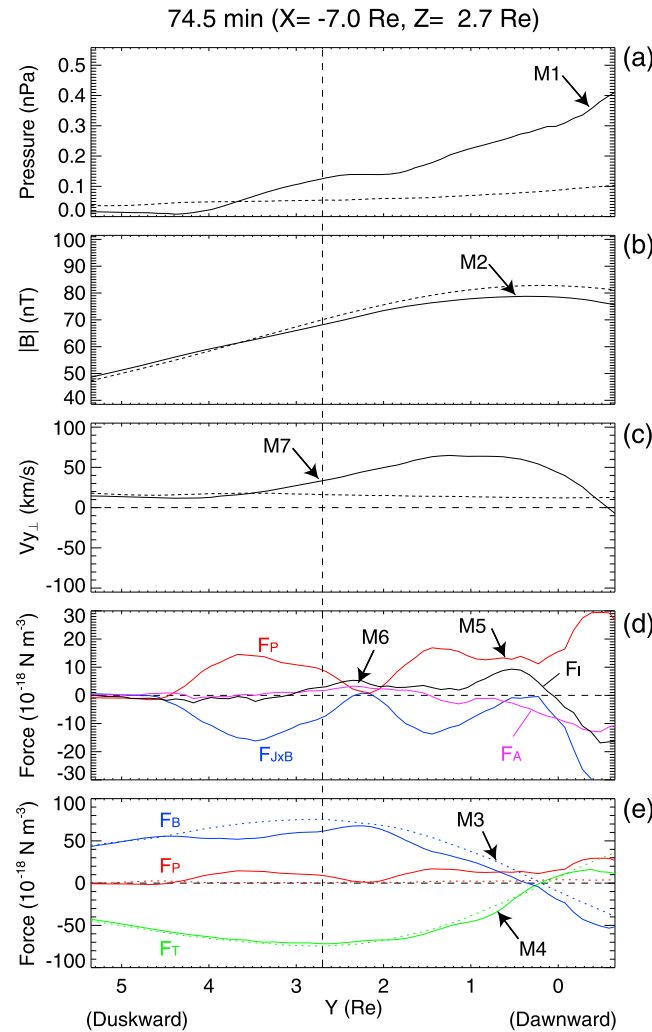


**Figure 8.** (a) Plasma pressure, (b) magnitude of the magnetic field, (c) the Y component of the perpendicular plasma velocity, (d) force densities (inertial force  $F_I$ , advection  $F_A$ , and plasma pressure force  $F_P$ ) and (4) force densities (plasma pressure force  $F_P$ , magnetic pressure force  $F_B$ , and tension force  $F_T$ ) at  $t = 74.5$  min. (e) The dotted line indicates the value taken at  $t = 65.5$  min.

understand the generation of the vorticity at the point P2 (which is connected to the WTS), we next focus on a point 0.30 Re closer to the equatorial plane, that is,  $(-7.00, 2.35, 2.70)$  Re.

Figure 8 is a summary of the pressure, the magnitude of the magnetic field, the Y component of the perpendicular velocity, and the Y component of the force density as a function of Y at  $X = -7.00$  and  $Z = 2.70$  Re. In an ideal MHD, the force density is given by

$$\begin{aligned}
 \mathbf{F}_I &= \mathbf{F}_A + \mathbf{F}_T + \mathbf{F}_B + \mathbf{F}_P, \\
 \mathbf{F}_I &= \rho \frac{\partial \mathbf{V}}{\partial t}, \\
 \mathbf{F}_A &= -\rho(\mathbf{V} \cdot \nabla) \mathbf{V}, \\
 \mathbf{F}_T &= \frac{1}{\mu_0}(\mathbf{B} \cdot \nabla) \mathbf{B}, \\
 \mathbf{F}_B &= -\nabla \left( \frac{B^2}{2\mu_0} \right), \\
 \mathbf{F}_P &= -\nabla P,
 \end{aligned} \tag{4}$$

and eastward. The configuration, pulling in and discharging ambient plasma, results in flow vortices, in addition to the global changes in the magnetospheric convection. Strong positive vorticity is found near the point P1, which generates upward FAC that manifests the initial brightening. The region of positive vorticity expands westward as time proceeds after the onset.

Figure 6 is the same as Figure 4 except for the FAC  $J_{\parallel}$ . Negative  $J_{\parallel}$  implies current flowing antiparallel to the magnetic field, that is, upward FAC in the Northern Hemisphere. At  $t = 69.5$  min (onset), strong upward FAC is found (Figure 6 P1) where the vorticity is strongly positive (Figure 5 P1). The current line extending from this region (Figure 6 P1) is connected to the ionosphere, resulting in a sudden increase in the upward FAC that manifests the initial brightening in the ionosphere (Figure 1). After the onset, the region of the upward FAC expands westward and eastward.

Figure 7 shows plasma pressure, the Y component of the perpendicular flow velocity, parallel vorticity, and FAC at  $(-7.00, 2.35, 3.00)$  Re. This point is labeled by P2 in Figures 4–6. During the period from the onset to  $t = 74.5$  min, the plasma pressure, the parallel vorticity, and the upward FAC increase significantly. The flow in the Y direction is almost unchanged during this period (probably due to the center of the shear or vorticity). In order to

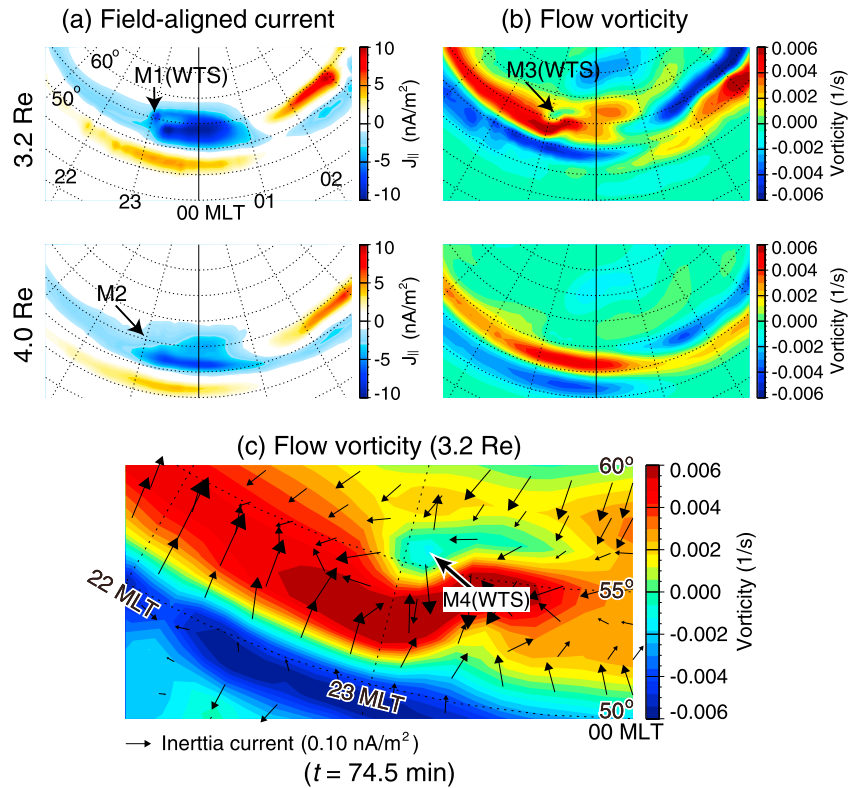


**Figure 9.** (a) Field-aligned current and (b) parallel vorticity in the magnetosphere at the geocentric distance of 3.2 Re and 4.0 Re at  $t = 74.5$  min. (c) Parallel vorticity at 3.2 Re with the arrows indicating the inertia current. Sun is to the top.

where  $\mathbf{F}_I$ ,  $\mathbf{F}_A$ ,  $\mathbf{F}_T$ ,  $\mathbf{F}_B$ , and  $\mathbf{F}_P$  are the inertial force, the force associated with advection, the tension force, the magnetic pressure force, and the plasma pressure force, respectively,  $\rho$  is the mass density of the plasma, and  $\mu_0$  is the magnetic constant. The Lorentz force  $\mathbf{F}_{\times B}$  is a sum of  $\mathbf{F}_T$  and  $\mathbf{F}_B$ . The solid line indicates the value at  $t = 74.5$  min, while the dotted line indicates the value at  $t = 65.5$  min. Before the onset, the total pressure force ( $\mathbf{F}_P + \mathbf{F}_B$ ) is almost balanced with the tension force ( $\mathbf{F}_T$ ), while after the onset, they are not balanced. Noticeable features can be summarized as follows: (1) The plasma pressure significantly increases (Figure 8 M1). (2) The intensity of the magnetic field decreases because of the diamagnetic effect (Figure 8 M2). (3) Due to the reduction in the magnetic field, the magnetic pressure force (looking duskward) is reduced (Figure 8 M3), whereas the (dawnward) tension force is almost unchanged, or slightly decreased (Figure 8 M4). The enhanced plasma pressure force (looking duskward) dominates the Lorentz force (Figure 8 M5). As a consequence, the inertial force is increased and the plasma is accelerated duskward near midnight. Due to advection, the inertial force increased on the duskside (Figure 8 M6). (4) The Y component of the perpendicular velocity increased at  $Y = 2.35$  Re (Figure 8 M7). The duskward flow generates the flow vorticity or shear (Figures 7c and 5 P2), and the upward FAC (Figure 6 P2).

### 3.3. Vertical Structure of WTS

Figure 9 shows the FAC and the parallel vorticity at radial distances of 3.2 Re and 4.0 Re in the magnetosphere at  $t = 74.5$  min. At 3.2 Re, the distribution of the FAC (Figure 9 M1) is almost identical to that found in the ionosphere (Figure 1 e). At 4.0 Re, the distribution of the FAC is somewhat different from that found at 3.2 Re and in the ionosphere. The WTS-like distribution is almost absent, and only a bulge-like structure of the upward FAC is identified (Figure 9 M2). In Figure 9b, parallel vorticities are present. At 3.2 Re, positive vorticity is widely distributed. A noticeable feature is that the positive vorticity was reduced and almost absent just inside the WTS (Figure 9 M3). This may imply that localized negative vorticity is overlaid on global positive vorticity at this altitude. The overlaid negative vorticity is not found at 4.0 Re. Figure 9c is a close-up view of Figure 9b. The arrow indicates the inertia current. There is a tendency that the inertia current flows away from the

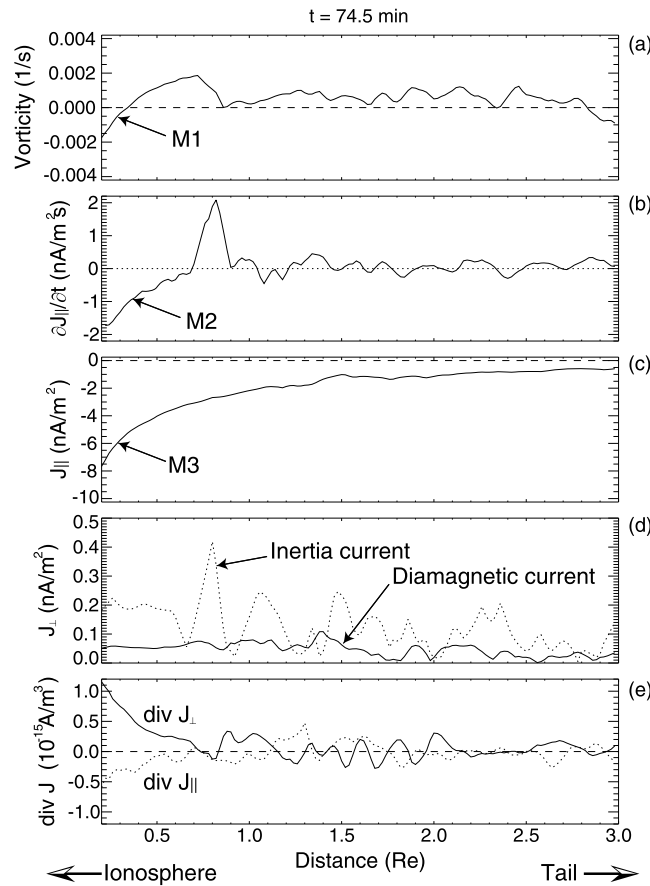


**Figure 10.** (a) Parallel vorticity, (b) generation rate of parallel current  $\partial J_{\parallel}/\partial t$ , (c) parallel current  $J_{\parallel}$ , (d) diamagnetic current (solid) and inertial current (dotted), and (e)  $\text{div } J_{\parallel}$  and  $\text{div } J_{\perp}$  as a function of distance from the leading edge of the WTS along a magnetic field line at  $t = 74.5$  min. The distance “0” corresponds to the radial distance of 3.0 Re.

center of the negative vorticity in the WTS (Figure 9 M4). The divergence of the inertial current may be suggestive of the (partial) closure of the upward FAC (Figure 9 M1).

We use Figure 10 to show the generation of the FAC and the continuity of the current at low altitude in the magnetosphere. The parallel vorticity  $\Omega_{\parallel}$  increases with distance from the WTS (Figure 10 M1) along a field line. According to equation (2), this favors generation of the upward FAC ( $\partial J_{\parallel}/\partial t < 0$ ) at low altitude (Figure 10 M2). The upward FAC ( $J_{\parallel} < 0$ ) is intensified at low altitude (Figure 10 M3). When integrating  $\partial J_{\parallel}/\partial t$  with respect to time (Figure 10b), one may notice that the integrated value is larger than  $J_{\parallel}$  (Figure 10c). The difference may come from the two reasons. One is that the generated FAC immediately propagates along a field line. The other one is that the Lorentz force immediately adjusts the force imbalance. In Figure 10d, it is shown that the magnitude of the inertial current dominates that of the diamagnetic current. In Figure 10e,  $\text{div } J_{\parallel}$  and  $\text{div } J_{\perp}$  are shown, where  $J_{\perp}$  is the perpendicular current being a sum of the diamagnetic current and the inertial current. At low altitude,  $\text{div } J_{\parallel}$  is negative, whereas  $\text{div } J_{\perp}$  is positive. These results

suggest that the upward FAC generated at low altitude is connected to the inertial current to maintain the current continuity. We note that the sum of  $\text{div } J_{\parallel}$  and  $\text{div } J_{\perp}$  is not exactly zero because of numerical error in computing  $\text{div } J_{\parallel}$  and  $\text{div } J_{\perp}$  in the low-beta region.

Figure 11 shows time variations of the force density in the X, Y, and Z components, the parallel vorticity, the parallel current, and the magnitude of the perpendicular current at the radial distance of 3.2 Re. This point is connected to the leading edge of the WTS along a field line at  $t = 74.5$  min. Just before the passage of the WTS (at  $t = 74.5$  min), the inertial force (black line) in the X and Z components increases, whereas that in the Y component decreases. This may be associated with the westward movement of the region of negative vorticity (Figure 9 M4). The inertial force is almost balanced with the Lorentz force, which is suggestive of the shear Alfvén wave. Since the negative flow vorticity is found at 3.2 Re and is absent at 4.0 Re (Figure 9), the vorticity should be driven at lower altitude by the Lorentz force (Figures 11a–11c). In Figures 11d and 11e, it is clearly shown that the parallel vorticity is minimum and the upward FAC is maximum when the WTS passes through this point. In Figure 11f, the inertial current appears to be intensified just before the passage of the WTS. The intensified inertial current is connected to the upward FAC generated at low altitude (Figure 10e).

### 3.4. Current Closure in the Ionosphere

Figure 12 shows distributions of the FAC, the ionospheric conductivity, the southward component of the ionospheric electric field, and the plasma pressure in the ionosphere at  $t = 74.5$  min. The plasma pressure is mapped from the inner boundary of the simulation domain. The WTS is located poleward of the Harang discontinuity, which is consistent with the observation [Weimer *et al.*, 1994]. We note that the ionospheric

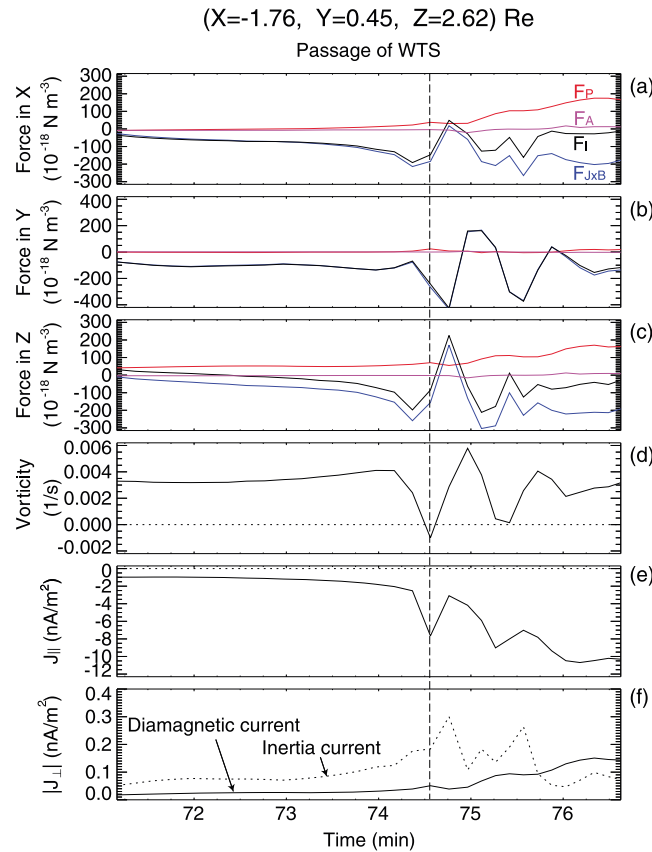


**Figure 11.** (a)  $X$  component of the force density, (b)  $Y$  component of the force density, (c)  $Z$  component of the force density, (d) parallel vorticity, (e) parallel current, and (f) divergence of the diamagnetic current (solid) and divergence of the inertial current (dotted) as a function of time. The vertical line indicates the moment at which the leading edge of the WTS passes through. In Figures 11a–11c, the red, blue, purple, and black lines indicate the plasma pressure force, the Lorentz force, the advection, and the inertia force, respectively.

electric potential is skewed on the leading edge of the WTS. That is, the ionospheric plasma drifting from the polar cap rotates counterclockwise on the leading edge of the WTS (Figure 12 M1). The counterclockwise rotation of the ionospheric plasma flow takes place near the gradient of the Hall conductivity (Figure 12 M2). In Figure 12c, the southward component of the electric field is present. The WTS appears in the southward electric field region (Figure 12 M3), which is consistent with observations [Fujii et al., 1994; Weimer et al., 1994]. The northward electric field (westward plasma flow) is found equatorward of the auroral oval (Figure 12 M4) and is known as subauroral ionization drift (SAID), subauroral electric field, or subauroral polarization stream [Galperin et al., 1973; Spiro et al., 1979; Anderson et al., 1991; Karlsson et al., 1998; Foster and Vo, 2002]. SAID was observed at the same time as the WTS [Fujii et al., 1994; Weimer et al., 1994]. The magnetospheric plasma pressure mapped to the ionosphere is present in Figure 10d. The pressure is high in the equatorward part of the bulge, which may reflect a manifestation of the central plasma sheet [Winningham et al., 1975]. This may also be consistent with observations that showed the equatorward part of the bulge being occupied by the central plasma sheet [Fujii et al., 1994].

Figure 13 shows the divergence of the Hall current  $J_H$ , the divergence of Pedersen current  $J_P$ , the ratio  $R=(\text{div } J_H + \text{div } J_P)/|\text{div } J_H|$ , and the divergence of the ionospheric electric field. The intensity of the Hall current is larger in the high-conductivity region (upward FAC region) than in the low-conductivity region, resulting in the gradient in the Hall current. The overflow of the Hall current ( $\text{div } J_H < 0$ ) occurs near the leading edge of the WTS (Figure 13 M1). Near the leading edge of the WTS,  $\text{div } J_P$  is positive with its magnitude being smaller than that of  $\text{div } J_H$ . This situation, in which  $\text{div } J_H < 0$ ,  $\text{div } J_P > 0$ , and the FAC is upward, may correspond to the case of Figure 5b in Fujii et al. [2011]. When the convergence of the Hall current is perfectly connected to the upward FAC, the ratio  $|R|$  is equal to 1. The ratio  $R$  is calculated to be  $\sim -0.9$  near the leading edge of the WTS (Figure 13 M2). This implies that a large part of the convergence of the Hall current is connected to the upward FAC. It should be emphasized that the convergence of the Hall current is not perfectly connected to the upward FAC. The remnant of the current is connected to the Pedersen current because  $\text{div } J_P > 0$ . The additional Pedersen current is essentially explained in terms of charge accumulation and is a cause of the Cowling channel [e.g., Baumjohann, 1982; Fujii et al., 2011]. The divergence of the ionospheric electric field is positive near the leading edge of the WTS (Figure 13 M3). The above process has already been suggested by Kan et al. [1984] in terms of a partial blockage of the Hall current. The positive divergence of the electric field implies that the ionospheric plasma drift counterclockwise around it (in the Northern Hemisphere). The counterclockwise flow near the leading edge of the WTS is found in Figure 12a (Figure 12 M1) and may be consistent with observations by a low-altitude satellite [Weimer et al., 1994, Figure 11]. In the simulation,

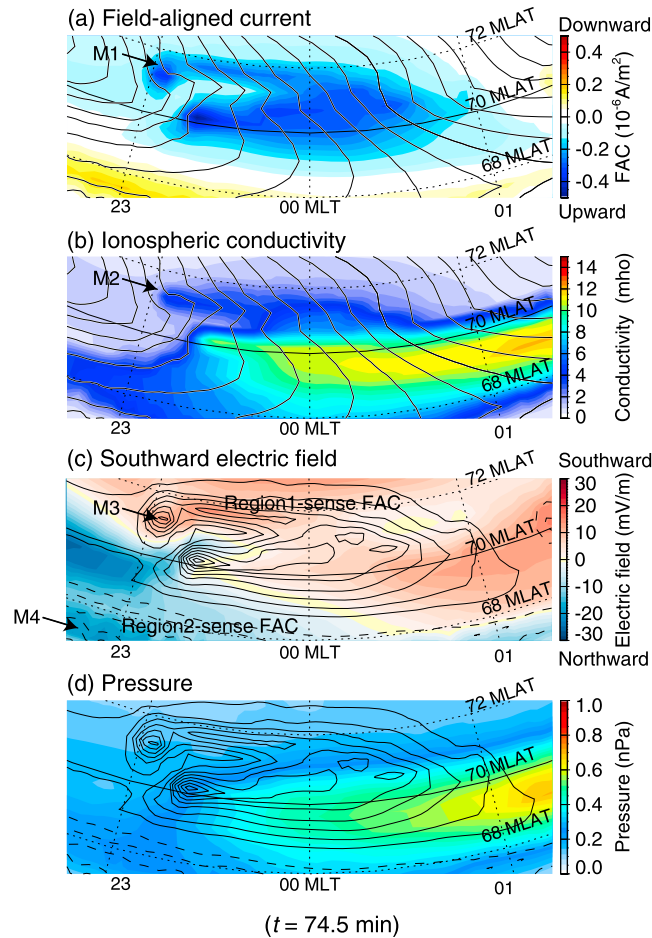


**Figure 12.** (a) Field-aligned current, (b) nondiagonal component of the ionospheric conductivity, (c) southward component of the ionospheric electric field, and (d) the ionospheric projection of the plasma pressure at  $t = 74.5$  min. The contour lines in Figures 12a and 12b indicate the ionospheric electric potential with an interval of 1 kV. The contour lines in Figures 12c and 12d indicate the field-aligned current with an interval of  $0.05 \mu\text{A}/\text{m}^2$ . The solid contour line denotes the upward current, and the dashed one denotes the downward current.

the divergent electric field is mapped to the inner boundary of the magnetosphere, corresponding to counterclockwise rotation of magnetospheric plasma (i.e., negative vorticity) at low altitude. At low altitude in the magnetosphere, the counterclockwise flow (negative vorticity) generates the upward FAC as shown in Figure 10.

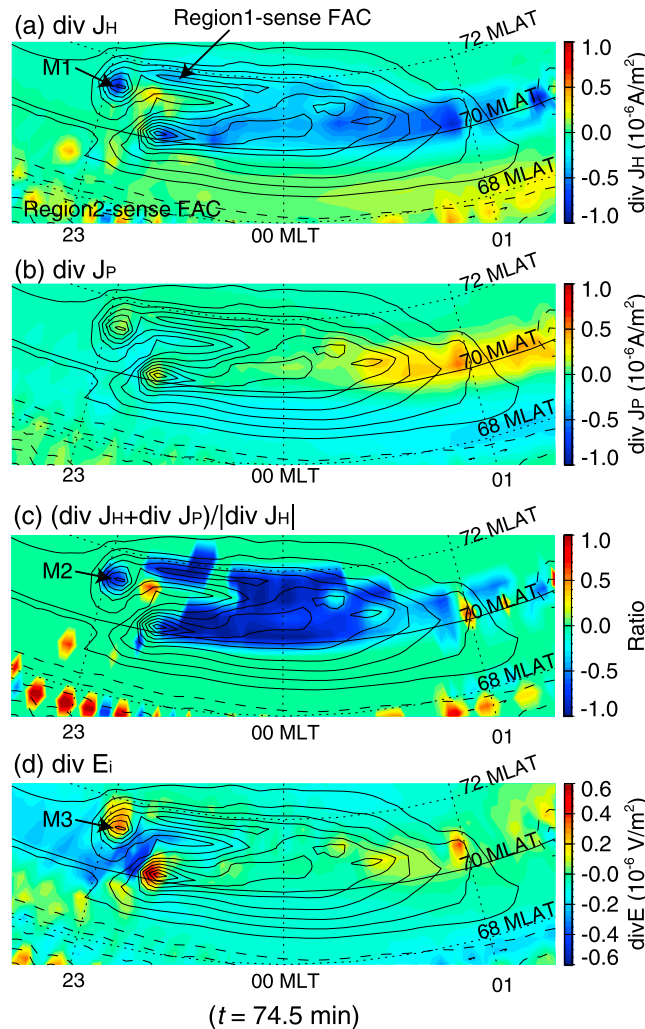
In Figure 14, the other current is extending from the downward FAC region equatorward of the WTS. This current line is regarded to as the Region 2-sense current. Some of the Region 2-sense current are connected to the perpendicular current (mostly the diamagnetic current) near the western edge of the high-pressure region. This is consistent with the current continuity condition suggested by Vasylunas [1984] and is pointed out by Tanaka et al. [2010].

Figure 15 is a schematic drawing of the current line associated with the WTS, based on the result obtained by the MHD simulation. After the onset, the high pressure continues to expand due to continued earthward fast flow in the plasma sheet. The high-pressure region at off-equator pulls in and discharges the ambient plasma, generating the positive vorticity ( $\Omega_{\parallel} > 0$ ; Vorticity I) in the westward and upper portion of the off-equatorial high-pressure region. Vorticity I generates the broad upward FAC that seems to have an important role in causing the primary electric field to flow the ionospheric currents. Because of the gradient of the ionospheric conductivity, the Hall current overflows in the ionosphere, resulting in the positive divergence of the electric field near the leading edge of the WTS in the ionosphere. The positive divergence of the electric field corresponds to counterclockwise rotation of plasma at the lower boundary of the

the divergent electric field is mapped to the inner boundary of the magnetosphere, corresponding to counterclockwise rotation of magnetospheric plasma (i.e., negative vorticity) at low altitude. At low altitude in the magnetosphere, the counterclockwise flow (negative vorticity) generates the upward FAC as shown in Figure 10.

### 3.5. 3-D Current System in the Magnetosphere

Figure 14 is a bird's-eye view of the three current lines at 74.5 min. Two currents are extending from the leading edge of the WTS (Current line I) and the wake of the WTS (Current line II). Both current lines are found to pass through the westside of the high-pressure region and contact the mantle. Along the current lines, there are at least two regions where  $\mathbf{J} \cdot \mathbf{E} < 0$  (dynamo): one at the tailward portion of the cusp (i.e., the mantle region or mantle dynamo) and the other in the near-Earth region at off-equator (near-Earth dynamo). The mantle dynamo is well documented by Janhunen et al. [1996], Tanaka [2000, 2007], Siscoe et al. [2000], and Tanaka et al. [2010] for explaining the generation of the Region 1 FAC. The near-Earth dynamo is additionally generated when the plasma pressure is enhanced in the inner magnetosphere (Paper 1) and is also suggested by Birn and Hesse [2005]. It should be noted that (1) the upward FAC extending from WTS is totally diverted from a magnetic field



**Figure 13.** (a) Divergence of the Hall current  $J_H$ , (b) divergence of the Pedersen current  $J_P$ , (c) the ratio  $R = (\text{div } J_H + \text{div } J_P) / \text{div } J_H$ , and (d) divergence of the ionospheric electric field. The contour lines indicate the field-aligned current with an interval of  $0.05 \mu\text{A}/\text{m}^2$ .

electric field) and generates clockwise flow around it. This will happen if the ionospheric conductivity is almost uniform. When the ionospheric conductivity is highly nonuniform (e.g., a leading edge of WTS), the Hall current is expected to overflow. When the convergence of the Hall current is not fully connected to the FAC, the divergence of the electric field becomes positive to generate the Pedersen current [Kan et al., 1984, 1988; Kan and Kamide, 1985; Fujii et al., 2011]. In our simulation, the positive divergence of the electric field and the counterclockwise flow appear on the leading edge of the WTS (Figure 10 M1) because of this process. The convergence of the Hall current is connected to the FAC and the Pedersen current, but the distribution ratio is uncertain as pointed out by Fujii et al. [2011]. The situation seems not to be so simple because the system is essentially self-consistent. It seems that a surge may be a natural consequence when the strong gradient of the conductivity and the strong primary electric field are present. In the WTS, the strong gradient of the conductivity is probably provided by the initial brightening (Paper 1), and the strong primary electric field is provided by the FACs. More observations are needed to confirm this scenario since Opgenoorth et al. [1983] showed counterclockwise Hall current (clockwise plasma flow) near the leading edge of a surge.

It may be speculated that a surge will not be developed well if the counterclockwise flow is absent in the ionosphere. The counterclockwise flow is generated by the overflow of the Hall current. This implies that sufficient gradient of the Hall conductivity must be provided at the initial brightening to initiate and develop

magnetosphere ( $\Omega_{\parallel} < 0$ ; Vorticity II). Vorticity II generates the fine-scale upward FAC, which is thinner than generated by Vorticity I, and may be a manifestation of the WTS. At the leading edge of the WTS, plasma starts to move counterclockwise. The inertial current flows in the radial direction away from the center of Vorticity II. The upward FAC generated at low altitude is, in part, connected to the inertial current. The remnant of the current will be connected to the magnetospheric dynamo. Because the diamagnetic current flows westward in the upper part of the off-equatorial high-pressure region, the current line extending from the WTS is deflected westward from a magnetic field line.

#### 4. Discussion

First, we discuss the relationship between the WTS and the ionospheric convection pattern. The ionospheric plasma appears to flow counterclockwise on the leading edge of the surge (Figure 10 M1). This is consistent with a schematic diagram presented by Weimer et al. [1994, Figure 11] who studied electric and magnetic fields, plasma drifts, and electron precipitation on the leading edge of WTS on the basis of the data from the DE 2 satellite. Marklund et al. [1998], however, argued the existence of the counterclockwise flow. They pointed out that the Weimer et al. [1994] model is inconsistent with the expectation that the upward FAC deposits negative charge (convergent

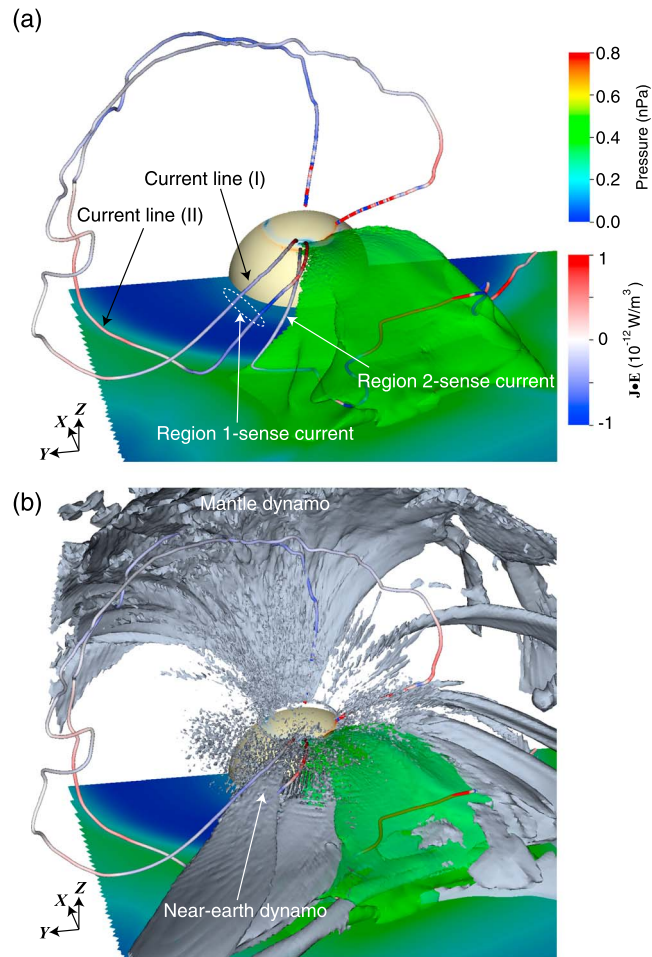


**Figure 14.** Snapshot of the current lines extending from the leading edge of the WTS (current line I) and the wake of the WTS (current line II) at  $t = 74.5$  min. A current line extending from the downward FAC region just equatorward of the WTS (Region 2-sense current) is also drawn. The current line is colored with the value of  $\mathbf{J} \cdot \mathbf{E}$ . The greenish surface is an iso-pressure surface at 0.4 nPa, and the grayish surface is an iso- $\mathbf{J} \cdot \mathbf{E}$  surface at  $-0.4 \times 10^{-12} \text{ W m}^{-3}$ . The horizontal plane shows the plasma pressure in the equatorial plane.

the WTS. In other words, “ignition” of the aurora (ionospheric conductivity) may be necessary at the onset. It is speculated that the degree of the gradient of the Hall conductivity at onset may determine breakups or pseudobreakups [Akasofu, 1964; Koskinen *et al.*, 1993; Ohtani *et al.*, 1993; Nakamura *et al.*, 1994; Rostoker, 1998]. The MHD simulation results predict that the upward FAC associated with the initial brightening is generated by the high-pressure region at off-equator (Paper 1). If this is the case, the plasma pressure (or scale length of the high-pressure region) will be one of the determining factors for the formation of the WTS. We can also speculate that the surge will not be developed in a sunlit ionosphere in which the electron production rate is completely dominated by solar radiation. This may be one of the reasons why discrete aurorae are suppressed in the sunlit ionosphere [Newell *et al.*, 1996]. A similar situation would occur during storm time because of continued precipitation of electrons and protons into the ionosphere. Hoffman *et al.* [2010] pointed out the lack of a surge and bulge during storm time substorms.

Downward FAC is observed by satellites just poleward of the WTS [Fujii *et al.*, 1994; Marklund *et al.*, 1998; Cummer *et al.*, 2000]. The downward FAC, referred to as Region 0 current, is thought to be a return current of the upward FAC of the WTS [Marklund *et al.*, 1998]. In our simulation, the Region 0-sense downward FAC is located poleward of the bulge (not on the leading edge of WTS). The current density is  $\sim 1$  order of magnitude smaller than the upward FAC of the WTS. If the Region 0 current is a return current of the upward FAC of the WTS, then the Region 0 current will be rapidly intensified when the WTS develops.

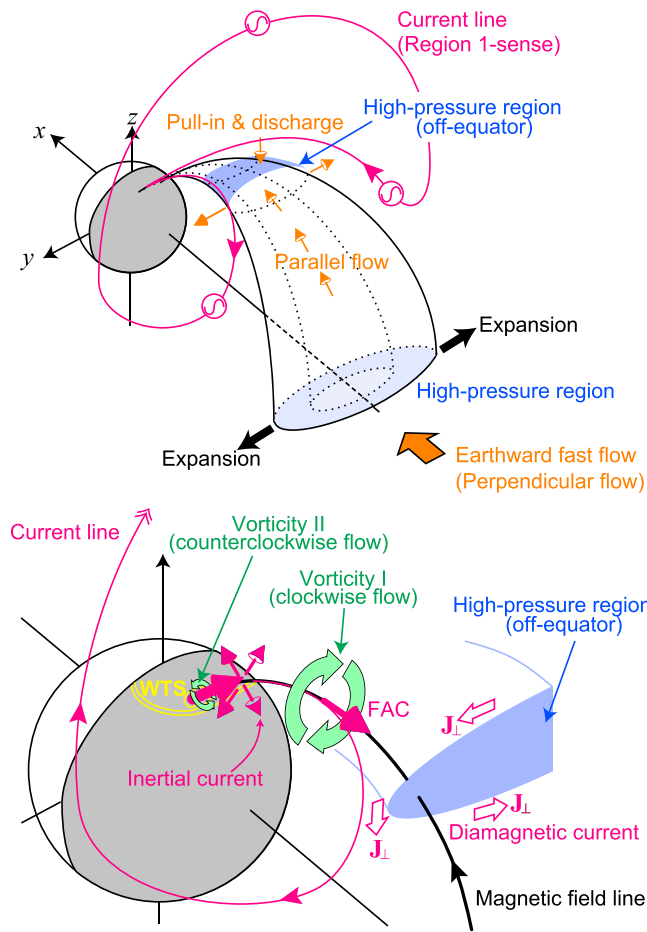


**Figure 15.** Schematic drawing of the relevant processes generating the WTS.  $J_{\perp}$  denotes the perpendicular current. The upward FAC related to the WTS is generated in two distinct regions. One is associated with the off-equatorial high-pressure region, and the other one is associated with the overflow of the Hall current. The plasma moves clockwise in the former region (Vorticity I), and the plasma moves counterclockwise in the latter region (Vorticity II) in the Northern Hemisphere. The current line extending from the WTS is connected to the mantle dynamo.

ing front of the high-pressure region. The ionospheric conductivity also continues to increase in the upward FAC region. The gradient of the conductivity gives rise to the overflow of the Hall current in the ionosphere. The convergence of the Hall current is largely connected to the FAC at the leading edge of the WTS. The remnant of the current is connected to the Pedersen current, resulting in divergent electric field. Due to the divergent electric field, the magnetospheric plasma moves counterclockwise at low altitude. Localized upward FAC is generated at low altitude, which may manifest a WTS.

3. The WTS may be associated with the upward FACs generated in two different ways. One is the large-scale upward FAC that generates the primary ionospheric electric field and the primary Hall current. The other one is the fine-scale upward FAC that is generated at low altitude as a consequence of the overflow of the Hall current. The latter FAC manifests the WTS and keeps generating a sharp gradient of the ionospheric conductivity as it moves westward. The ionospheric current is then redistributed. The WTS may be a natural consequence of a steep gradient of the ionospheric conductance and the overflow of the Hall current. It can be said that the WTS is primarily maintained by the near-Earth high-pressure region and the magnetosphere-ionosphere coupling in a self-consistent manner.

However, the Region 0-sense downward FAC remains to exist in the late growth phase and the expansion phase in the simulation. *Watanabe and Iijima* [1993] found that the Region 0 current appears in the evening sector during the substorm growth phase. The temporal evolution of the Region 0 current and its role in the formation of the WTS remain unclear and to be solved.

### 5. Conclusions

In this study, MHD simulation results were used to investigate the formation of WTS. Major conclusions can be summarized as follows:

1. After the formation of the near-Earth neutral line (NENL), magnetic tension is released in the near-Earth plasma sheet to compress and accelerate plasma earthward. High-pressure region is formed in the inner magnetosphere. Flow vorticities are generated near the off-equatorial high-pressure region. The resultant field-aligned current (FAC) is connected to the ionosphere, which may manifest the initial brightening.
2. Due to magnetic tension and continued earthward flow, the region of high pressure continues to expand toward east and west forming the configuration of partial ring current. Near-Earth high-pressure region continues to develop at the expand-

### Acknowledgments

We thank Takashi Kikuchi, Takeshi Sakanoi, Akimasa Ieda, and Kazuo Shiokawa for fruitful comments and discussion. The computer simulation was performed on the KDK computer system at the Research Institute for Sustainable Humanosphere (RISH), Kyoto University. This study was supported by KAKENHI (grants 24340119, 15H03732, and 15H05815). The simulation data are available upon request.

### References

- Akasofu, S.-I. (1963), The dynamical morphology of the aurora polaris, *J. Geophys. Res.*, *68*, 1667–1673, doi:10.1029/JZ068i006p01667.
- Akasofu, S.-I. (1964), The development of the auroral substorm, *Planet. Space Sci.*, *12*, 273–282, doi:10.1016/0032-0633(64)90151-5.
- Akasofu, S.-I., D. S. Kimball, and C.-I. Meng (1965), The dynamics of the aurora. II. Westward traveling surges, *J. Atmos. Terr. Phys.*, *27*, 173–187, doi:10.1016/0021-9169(65)90114-5.
- Akasofu, S.-I., R. H. Eather, and J. N. Bradbury (1969), The absence of the hydrogen emission (H $\beta$ ) in the westward traveling surge, *Planet. Space Sci.*, *17*, 1409, doi:10.1016/0032-0633(69)90207-4.
- Akasofu, S.-I., E. W. Hones Jr., M. D. Montgomery, S. J. Bame, and S. Singer (1971), Association of magnetotail phenomena with visible auroral features, *J. Geophys. Res.*, *76*, 5985–6003, doi:10.1029/JA076i025p05985.
- Anderson, P. C., R. A. Heelis, and W. B. Hanson (1991), The ionospheric signatures of rapid subauroral ion drifts, *J. Geophys. Res.*, *96*, 5785–5792, doi:10.1029/90JA02651.
- Angelopoulos, V., C. F. Kennel, F. V. Coroniti, R. Pellat, M. G. Kivelson, R. J. Walker, C. T. Russell, W. Baumjohann, W. C. Feldman, and J. T. Gosling (1994), Statistical characteristics of bursty bulk flow events, *J. Geophys. Res.*, *99*(A11), 21,257–21,280, doi:10.1029/94JA01263.
- Anger, C. D., A. T. Y. Lui, and S.-I. Akasofu (1973), Observations of the auroral oval and a westward traveling surge from the ISIS 2 satellite and the Alaskan meridian all-sky cameras, *J. Geophys. Res.*, *78*, 3020–3026, doi:10.1029/JA078i016p03020.
- Baker, D. N., T. I. Pulkkinen, V. Angelopoulos, W. Baumjohann, and R. L. McPherron (1996), Neutral line model of substorms: Past results and present view, *J. Geophys. Res.*, *101*(A6), 12,975–13,010, doi:10.1029/95JA03753.
- Baumjohann, W. (1982), Ionospheric and field-aligned current system in the auroral zone: A concise review, *Adv. Space Res.*, *2*(10), 55–62, doi:10.1016/0273-1177(82)90363-5.
- Baumjohann, W. (1983), Ionospheric and field-aligned current systems in the auroral zone: A concise review, *Adv. Space Res.*, *2*, 55–62, doi:10.1016/0273-1177(82)90363-5.
- Baumjohann, W. J., and H. J. Opgenoorth (1984), Electric fields and currents associated with active aurora, in *Magnetospheric Currents*, *Geophys. Monogr. Ser.*, vol. 28, edited by T. A. Potemra, pp. 77–85, AGU, Washington, D. C.
- Baumjohann, W., R. J. Pellinen, H. J. Opgenoorth, and E. Nielsen (1981), Joint two-dimensional observations of ground magnetic and ionospheric electric fields associated with auroral zone currents: Current systems associated with local auroral break-ups, *Planet. Space Sci.*, *29*, 431, doi:10.1016/0032-0633(81)90087-8.
- Birn, J., and M. Hesse (1996), Details of current disruption and diversion in simulations of magnetotail dynamics, *J. Geophys. Res.*, *101*(A7), 15,345–15,358, doi:10.1029/96JA00887.
- Birn, J., and M. Hesse (2005), Energy release and conversion by reconnection in the magnetotail, *Ann. Geophys.*, *23*, 3365–3373.
- Birn, J., and M. Hesse (2013), The substorm current wedge in MHD simulations, *J. Geophys. Res. Space Physics*, *118*, 3364–3376, doi:10.1002/jgra.50187.
- Birn, J., M. Hesse, G. Haerendel, W. Baumjohann, and K. Shiokawa (1999), Flow braking and the substorm current wedge, *J. Geophys. Res.*, *104*(A9), 19,895–19,903, doi:10.1029/1999JA000173.
- Birn, J. M., et al. (2004), On the propagation of bubbles in the magnetotail, *Ann. Geophys.*, *22*, 1773–1786.
- Boström, R. (1975), Mechanisms for driving Birkeland currents, in *Physics of the Hot Plasma in the Magnetosphere*, edited by B. Hultqvist and L. Stenflo, pp. 431–447, Plenum, New York.
- Bythrow, P. F., and T. A. Potemra (1987), Birkeland currents and energetic particles associated with optical auroral signatures of a westward traveling surge, *J. Geophys. Res.*, *92*(A8), 8691–8699, doi:10.1029/JA092iA08p08691.
- Cowley, S. W. H. (1981), Magnetospheric asymmetries associated with the y-component of the IMF, *Planet. Space Sci.*, *29*, 79–96, doi:10.1016/0032-0633(81)90141-0.
- Craven, J. D., L. A. Frank, and S.-I. Akasofu (1989), Propagation of a westward traveling surge and the development of persistent auroral features, *J. Geophys. Res.*, *94*(A6), 6961–6967, doi:10.1029/JA094iA06p06961.
- Cummer, S. A., et al. (2000), Auroral surge currents and electrodynamic with FAST and VIS, in *Magnetospheric Current Systems*, *AGU Geophys. Monogr.*, vol. 118, edited by S.-I. Ohtani et al., pp. 191–198, AGU, Washington, D. C., doi:10.1029/GM118p0191.
- Ebihara, Y., and T. Tanaka (2015), Substorm simulation: Insight into the mechanisms of initial brightening, *J. Geophys. Res. Space Physics*, *120*, 7270–7288, doi:10.1002/2015JA021516.
- Ebihara, Y., T. Tanaka, and T. Kikuchi (2014), Counter equatorial electrojet and overshielding after substorm onset: Global MHD simulation study, *J. Geophys. Res. Space Physics*, *119*, 7281–7296, doi:10.1002/2014JA020065.
- Elphinstone, R. D., et al. (1995), Observations in the vicinity of substorm onset: Implications for the substorm process, *J. Geophys. Res.*, *100*(A5), 7937–7969, doi:10.1029/94JA02938.
- Foster, J. C., and H. B. Vo (2002), Average characteristics and activity dependence of the subauroral polarization stream, *J. Geophys. Res.*, *107*(A12), 1475, doi:10.1029/2002JA009409.
- Fujii, R., R. A. Hoffman, P. C. Anderson, J. D. Craven, M. Sugiura, L. A. Frank, and N. C. Maynard (1994), Electrodynamic parameters in the nighttime sector during auroral substorms, *J. Geophys. Res.*, *99*(A4), 6093–6112, doi:10.1029/93JA02210.
- Fujii, R., O. Amm, A. Yoshikawa, A. Ieda, and H. Vanhamäki (2011), Reformulation and energy flow of the Cowling channel, *J. Geophys. Res.*, *116*, A02305, doi:10.1029/2010JA015989.
- Fukunishi, H. (1975), Dynamic relationship between proton and electron auroral substorms, *J. Geophys. Res.*, *8*(4), 553–574, doi:10.1029/JA080i004p00553.
- Galperin, Y. I., V. N. Ponomarev, and A. G. Zosimova (1973), Direct measurements of drift rate of ions in upper atmosphere during a magnetic storm. II. Results of measurements during magnetic storm of November 3, 1967, *Cosmic Res.*, *11*, 249–258.
- Haerendel, G. (2010), Equatorward moving arcs and substorm onset, *J. Geophys. Res.*, *115*, A07212, doi:10.1029/2009JA015117.
- Hoffman, R. A., J. W. Gjerloev, L. A. Frank, and J. W. Sigwarth (2010), Are there optical differences between storm-time substorms and isolated substorms?, *Ann. Geophys.*, *28*(5), 1183–1198.
- Ieda, A., S. Machida, T. Mukai, Y. Saito, T. Yamamoto, A. Nishida, T. Terasawa, and S. Kokubun (1998), Statistical analysis of the plasmoid evolution with Geotail observations, *J. Geophys. Res.*, *103*, 4453–4465, doi:10.1029/97JA03240.
- Inhester, B. W., W. Baumjohann, R. A. Greenwald, and E. Nielsen (1981), Joint two-dimensional observations of ground magnetic and ionospheric electric fields associated with auroral zone currents during the passage of a westward travelling surge, *J. Geophys.*, *49*, 155–162.
- Janhunen, P., H. E. J. Koskinen, and T. I. Pulkkinen (1996), A new global ionosphere-magnetosphere coupling simulation utilizing locally varying time step, in *Proceedings of the Third International Conference on Substorms (ICS-3)*, *ESA SP-389*, pp. 205–210, ESA SP, Paris.
- Juusola, L., N. Østgaard, E. Tanskanen, N. Partamies, and K. Snekvik (2011), Earthward plasma sheet flows during substorm phases, *J. Geophys. Res.*, *116*, A10228, doi:10.1029/2011JA016852.

- Kadokura, A., A.-S. Yukimatu, M. Ejiri, T. Oguti, M. Pinnock, and P. R. Sutcliffe (2002), Detailed analysis of a substorm event on 6 and 7 June 1989: 2. Stepwise auroral bulge evolution during expansion phase, *J. Geophys. Res.*, *107*(A12), 1480, doi:10.1029/2001JA009129.
- Kamide, Y., and S.-I. Akasofu (1975), The auroral electrojet and global auroral features, *J. Geophys. Res.*, *80*(25), 3585–3602, doi:10.1029/JA080i025p03585.
- Kan, J. R., and Y. Kamide (1985), Electrodynamics of the westward traveling surge, *J. Geophys. Res.*, *90*(A8), 7615–7619, doi:10.1029/JA090iA08p07615.
- Kan, J. R., R. L. Williams, and S.-I. Akasofu (1984), A mechanism for the westward traveling surge during substorms, *J. Geophys. Res.*, *89*(A4), 2211–2216, doi:10.1029/JA089iA04p02211.
- Kan, J. R., L. Zhu, and S.-I. Akasofu (1988), A theory of substorms: Onset and subsidence, *J. Geophys. Res.*, *93*(A6), 5624–5640, doi:10.1029/JA093iA06p05624.
- Karlsson, T., G. Marklund, L. Blomberg, and A. Mälkki (1998), Subauroral electric fields observed by the Freja satellite: A statistical study, *J. Geophys. Res.*, *103*, 4327–4341, doi:10.1029/97JA00333.
- Keiling, A., et al. (2009), Substorm current wedge driven by plasma flow vortices: THEMIS observations, *J. Geophys. Res.*, *114*, A00C22, doi:10.1029/2009JA014114.
- Kepko, L., R. L. McPherron, O. Amm, S. Apatenkov, W. Baumjohann, J. Birn, M. Lester, R. Nakamura, T. I. Pulkkinen, and V. Sergeev (2014), Substorm current wedge revisited, *Space Sci. Rev.*, doi:10.1007/s11214-014-0124-9.
- Koskinen, H. E. J., R. E. Lopez, R. J. Pellinen, T. I. Pulkkinen, D. N. Baker, and T. Bösinger (1993), Pseudobreakup and substorm growth phase in the ionosphere and magnetosphere, *J. Geophys. Res.*, *98*, 5801–5813, doi:10.1029/92JA02482.
- Lyons, L. R., Y. Nishimura, B. Gallardo-Lacourt, Y. Zou, E. Donovan, S. Mende, V. Angelopoulos, J. M. Ruohoniemi, and K. McWilliams (2013), Westward traveling surges: Sliding along boundary arcs and distinction from onset arc brightening, *J. Geophys. Res. Space Physics*, *118*, 7643–7653, doi:10.1002/2013JA019334.
- Machida, S., Y. Miyashita, A. Ieda, A. Nishida, T. Mukai, Y. Saito, and S. Kokubun (1999), GEOTAIL observations of flow velocity and north-south magnetic field variations in the near and mid-distant tail associated with substorm onsets, *Geophys. Res. Lett.*, *26*, 635–638, doi:10.1029/1999GL900030.
- Marklund, G. T., et al. (1998), Observations of the electric field fine structure associated with the westward traveling surge and large-scale auroral spirals, *J. Geophys. Res.*, *103*, 4125–4144, doi:10.1029/97JA00558.
- McPherron, R. L., C. T. Russell, and M. P. Aubry (1973), Satellite studies of magnetospheric substorms on August 15, 1968: 9. Phenomenological model for substorms, *J. Geophys. Res.*, *78*, 3131–3149, doi:10.1029/JA078i016p03131.
- Meng, C.-I., A. L. Snyder Jr., and H. W. Kroehl (1978), Observations of auroral westward traveling surges and electron precipitations, *J. Geophys. Res.*, *83*, 575–585, doi:10.1029/JA083iA02p00575.
- Nagai, T., M. Fujimoto, Y. Saito, S. Machida, T. Terasawa, R. Nakamura, T. Yamamoto, T. Mukai, A. Nishida, and S. Kokubun (1998), Structure and dynamics of magnetic reconnection for substorm onsets with Geotail observations, *J. Geophys. Res.*, *103*(A3), 4419–4440, doi:10.1029/97JA02190.
- Nakamura, R., D. N. Baker, T. Yamamoto, R. D. Belian, E. A. Bering III, J. R. Benbrook, and J. R. Theall (1994), Particle and field signatures during pseudobreakup and major expansion onset, *J. Geophys. Res.*, *99*, 207–221, doi:10.1029/93JA02207.
- Newell, P. T., C.-I. Meng, and K. M. Lyons (1996), Discrete aurorae are suppressed in sunlight, *Nature*, *381*, 766, doi:10.1038/381766a0.
- Nishida, A. (1968), Coherence of geomagnetic DP 2 fluctuations with interplanetary magnetic variations, *J. Geophys. Res.*, *73*(17), 5549–5559, doi:10.1029/JA073i017p05549.
- Nishida, A., and N. Nagayama (1973), Synoptic survey for the neutral line in the magnetotail during the substorm expansion phase, *J. Geophys. Res.*, *78*, 3782–3798, doi:10.1029/JA078i019p03782.
- Ohtani, S., et al. (1993), A multisatellite study of a pseudo-substorm onset in the near-Earth magnetotail, *J. Geophys. Res.*, *98*(A11), 19,355–19,367, doi:10.1029/93JA01421.
- Olsson, A., M. A. L. Persson, H. J. Opgenoorth, and S. Kirkwood (1996), Particle precipitation in auroral breakups and westward traveling surges, *J. Geophys. Res.*, *101*, 24,661–24,673, doi:10.1029/96JA01748.
- Opgenoorth, H. J., R. J. Pellinen, W. Baumjohann, E. Nielsen, G. Marklund, and L. Eliasson (1983), Three-dimensional current flow and particle precipitation in a westward travelling surge (observed during the Barium-GEOS rocket experiment), *J. Geophys. Res.*, *88*, 3138–3152, doi:10.1029/JA088iA04p03138.
- Paschmann, G., S. Haaland, and R. Treumann (Eds.) (2002), *Auroral Plasma Physics*, Kluwer Acad., Boston/Dordrecht/London.
- Réme, H., and J. M. Bosqued (1973), Rocket observations of electron precipitation in a westward traveling surge, *J. Geophys. Res.*, *78*, 5553–5558, doi:10.1029/JA078i025p05553.
- Robinson, R. M., and R. R. Vondrak (1990), Electrodynamics properties of auroral surges, *J. Geophys. Res.*, *95*, 7819–7832, doi:10.1029/JA095iA06p07819.
- Rostoker, G. (1998), On the place of the pseudo-breakup in a magnetospheric substorm, *Geophys. Res. Lett.*, *25*, 217–220, doi:10.1029/97GL03583.
- Rostoker, G., A. Vallance Jones, R. L. Gattinger, C. D. Anger, and J. S. Murphree (1987), The development of the substorm expansive phase: The “eye” of the substorm, *Geophys. Res. Lett.*, *14*, 399–402, doi:10.1029/GL014i004p00399.
- Rothwell, P. L., M. B. Silevitch, and L. P. Block (1984), A model for the propagation of the westward traveling surge, *J. Geophys. Res.*, *89*, 8941–8948, doi:10.1029/JA089iA10p08941.
- Rothwell, P. L., M. B. Silevitch, L. P. Block, and P. Tanskanen (1988), A model of the westward traveling surge and the generation of Pi 2 pulsations, *J. Geophys. Res.*, *93*, 8613–8624, doi:10.1029/JA093iA08p08613.
- Russell, C. T., and R. L. McPherron (1973), The magnetotail and substorms, *Space Sci. Rev.*, *15*, 205–266, doi:10.1007/BF00169321.
- Saita, S., et al. (2011), Displacement of conjugate points during a substorm in a global magnetohydrodynamic simulation, *J. Geophys. Res.*, *116*, A06213, doi:10.1029/2010JA016155.
- Shiokawa, K., and H. Fukunishi (1991), Global characteristics of field-aligned acceleration processes associated with auroral arcs, *J. Geomag. Geoelectr.*, *43*, 691–719.
- Siscoe, G. L., N. U. Crooker, G. M. Erickson, B. U. Ö. Sonnerup, K. D. Siebert, D. R. Weimer, W. W. White, and N. C. Maynard (2000), Global geometry of magnetospheric currents inferred from MHD simulations, in *Magnetospheric Current Systems*, edited by S.-I. Ohtani et al., AGU, Washington, D. C., doi:10.1029/GM118p0041.
- Spiro, R. W., R. A. Heelis, and W. B. Hanson (1979), Rapid subauroral ion drifts observed by Atmospherics Explorer C, *Geophys. Res. Lett.*, *6*, 65–660, doi:10.1029/GL006i008p00657.
- Tanaka, T. (1994), Finite volume TVD scheme on an unstructured grid system for three-dimensional MHD simulation of inhomogeneous systems including strong background potential fields, *J. Comput. Phys.*, *111*, 381, doi:10.1006/jcph.1994.1071.

- Tanaka, T. (2000), Field-aligned current systems in the numerically simulated magnetosphere, in *Magnetospheric Current Systems*, *Geophys. Monogr. Ser.*, vol. 118, edited by S. Ohtani et al., p. 53, AGU, Washington, D. C.
- Tanaka, T. (2007), Magnetosphere-ionosphere convection as a compound system, *Space Sci. Rev.*, 133, 1, doi:10.1007/s11214-007-9168-4.
- Tanaka, T. (2015), Substorm auroral dynamics reproduced by the advanced global M-I coupling simulation, in *Auroral Dynamics and Space Weather*, *Geophys. Monogr. Ser.*, vol. 215, edited by Y. Zhang and L. J. Paxton, pp. 177–192, AGU, Washington, D. C.
- Tanaka, T., A. Nakamizo, A. Yoshikawa, S. Fujita, H. Shinagawa, H. Shimazu, T. Kikuchi, and K. K. Hashimoto (2010), Substorm convection and current system deduced from the global simulation, *J. Geophys. Res.*, 115, A05220, doi:10.1029/2009JA014676.
- Vasyliunas, V. M. (1984), Fundamentals of current description, in *Magnetospheric Currents*, edited by T. A. Potemra, AGU, Washington, D. C., doi:10.1029/GM028p0063.
- Vogt, J. (2002), Alfvén wave coupling in the auroral current circuit, *Surv. Geophys.*, 23(4), 335–377.
- Watanabe, M., and T. Iijima (1993), Substorm growth phase on the magnetotail, *J. Geophys. Res.*, 98, 17,299–17,316, doi:10.1029/93JA01474.
- Weimer, D. R., J. D. Craven, L. A. Frank, W. B. Hanson, N. C. Maynard, R. A. Hoffman, and J. A. Slavin (1994), Satellite measurements through the center of a substorm surge, *J. Geophys. Res.*, 99, 23,639–23,649, doi:10.1029/94JA01976.
- Winningham, J. D., F. Yasuhara, S.-I. Akasofu, and W. J. Heikkila (1975), The latitudinal morphology of 10-eV to 10-keV electron fluxes during magnetically quiet and disturbed times in the 2100–0300 MLT sector, *J. Geophys. Res.*, 80, 3148–3171, doi:10.1029/JA080i022p03148.
- Yao, Z. H., et al. (2012), Mechanism of substorm current wedge formation: THEMIS observations, *Geophys. Res. Lett.*, 39, L13102, doi:10.1029/2012GL052055.
- Yoshikawa, A., O. Amm, H. Vanhamäki, and R. Fujii (2011), A self-consistent synthesis description of magnetosphere-ionosphere coupling and scale-dependent auroral process using shear Alfvén wave, *J. Geophys. Res.*, 116, A08218, doi:10.1029/2011JA016460.